Microphysical effects determine macrophysical response for aerosol impacts on deep convective clouds

Jiwen Fan[a,1], L. Ruby Leung[a], Daniel Rosenfeld[b], Qian Chen[a,c], Zhanqing Li[d,e], Jinqiang Zhang[f], and Hongru Yan[e,g]

[a]Atmospheric Sciences and Global Change Division, Pacific Northwest National Laboratory, Richland, WA 99352; [b]Institute of Earth Sciences, The Hebrew University of Jerusalem, Jerusalem, 91904 Israel; [c]Key Laboratory for Aerosol-Cloud-Precipitation of China Meteorological Administration, Nanjing University of Information Science and Technology, Nanjing 210044, China; [d]State Key Laboratory of Earth Surface Processes and Resource Ecology, College of Global Change and Earth System Science, Beijing Normal University, Beijing 100875, China; [e]Department of Atmospheric and Oceanic Science and Earth System Science Interdisciplinary Center, University of Maryland, College Park, MD 20742; [f]Key Laboratory of the Middle Atmosphere and Global Environmental Observation, Institute of Atmospheric Physics, Chinese Academy of Sciences, Beijing 100029, China; and [g]College of Atmospheric Sciences, Lanzhou University, Lanzhou, China

Edited by Mark H. Thiemens, University of California, San Diego, La Jolla, CA, and approved October 22, 2013 (received for review September 10, 2013)

Deep convective clouds (DCCs) play a crucial role in the general circulation, energy, and hydrological cycle of our climate system. Aerosol particles can influence DCCs by altering cloud properties, precipitation regimes, and radiation balance. Previous studies reported both invigoration and suppression of DCCs by aerosols, but few were concerned with the whole life cycle of DCC. By conducting multiple monthlong cloud-resolving simulations with spectral-bin cloud microphysics that capture the observed macrophysical and microphysical properties of summer convective clouds and precipitation in the tropics and midlatitudes, this study provides a comprehensive view of how aerosols affect cloud cover, cloud top height, and radiative forcing. We found that although the widely accepted theory of DCC invigoration due to aerosol's thermodynamic effect (additional latent heat release from freezing of greater amount of cloud water) may work during the growing stage, it is microphysical effect influenced by aerosols that drives the dramatic increase in cloud cover, cloud top height, and cloud thickness at the mature and dissipation stages by inducing larger amounts of smaller but longer-lasting ice particles in the stratiform/anvils of DCCs, even when thermodynamic invigoration of convection is absent. The thermodynamic invigoration effect contributes up to ∼27% of total increase in cloud cover. The overall aerosol indirect effect is an atmospheric radiative warming (3–5 W·m^{-2}) and a surface cooling (−5 to −8 W·m^{-2}). The modeling findings are confirmed by the analyses of ample measurements made at three sites of distinctly different environments.

aerosol–cloud interactions | aerosol indirect forcing

Deep convective clouds (DCCs), particularly those associated with tropical convection, are significant sources of precipitation and play a key role in the hydrological and energy cycle as well as regional and global circulation (1). DCCs are organized into one or more convective cores characterized by strong updrafts that merge at the mature phase and anvil clouds that result from divergence of the updrafts from the convective cores just below the tropopause and spread over large areas. Cloud top height (CTH), cloud thickness, and microphysical properties are important properties of DCCs that influence their radiation effects. Satellite radar observations show a correlation between convective intensity and lifetime, size, and depth of the anvils (2). Because of their large coverage and long lifetime, anvils dominate the radiative effects of DCCs.

Atmospheric aerosol particles can influence cloud properties and precipitation regimes through their impacts on cloud microphysical and macrophysical processes and consequently alter the radiation balance of the climate system. These so-called aerosol indirect effects remain a key uncertainty in understanding the current and future climate (3). Quantifying aerosol impacts on DCCs is exceptionally challenging because the interactions among cloud microphysics (liquid, ice, and mixed-phase), radiation, and atmospheric dynamics are very complex and cover a wide range of spatial and temporal scales (4).

Previous modeling studies on aerosol–DCC interactions focusing on how aerosols modify convection intensity and precipitation (4) show discrepancies in both the sign and magnitude (5–14). By explicitly resolving convection, cloud-resolving models can produce more realistic structures of DCCs than coarser-scale models that rely on convective parameterizations. Cloud-resolving model (CRM) simulations have identified the role of environmental conditions such as vertical wind shear and relative humidity (RH) (5–10, 14) as key factors in determining whether aerosols enhance or suppress convection intensity. One-month idealized 2-D simulations with two-moment bulk microphysics over tropics showed higher CTH despite weaker convection in the polluted environment (15) and suggested an effect from microphysical changes by increasing cloud condensation nuclei (CCN). Very recent idealized modeling studies using radiative–convective equilibrium for tropical convection showed that cloud fraction is changed very little by CCN (16, 17), and both shortwave (SW) and longwave (LW) radiative forcings at the top of atmosphere (TOA) are reduced by CCN (17).

In contrast, observational studies have consistently showed increased CTH and cloud fractions and higher precipitation rates in polluted environments over large regions (18–22) and globally (23) at long time scales (months and years). To explain the ob-

Significance

Deep convective clouds (DCCs) play a key role in atmospheric circulation and the hydrological and energy cycle. How aerosol particles affect DCCs is poorly understood, making it difficult to understand current and future weather and climate. Our work showed that in addition to the invigoration of convection, which has been unanimously cited for explaining the observed results, the microphysical effects induced by aerosols are a fundamental reason for the observed increases in cloud fraction, cloud top height, and cloud thickness in the polluted environment, even when invigoration is absent. The finding calls for an augmented focus on understanding the changes in stratiform/anvils associated with convective life cycle.

Author contributions: J.F. designed research; J.F. performed research; J.F., Q.C., J.Z., and H.Y. analyzed data; and J.F., L.R.L., D.R., and Z.L. wrote the paper.

The authors declare no conflict of interest.

This article is a PNAS Direct Submission.

Freely available online through the PNAS open access option.

[1]To whom correspondence should be addressed. E-mail: jiwen.fan@pnnl.gov.

This article contains supporting information online at www.pnas.org/lookup/suppl/doi:10.1073/pnas.1316830110/-/DCSupplemental.

served higher cloud top and larger cloud fraction in polluted environments, a common hypothesis put forth in those studies is that aerosols delay conversion of cloud water to warm rain due to reduced cloud drop size, allowing larger amounts of cloud water to be lifted to the upper levels that, upon freezing, release more latent heat and invigorate convection (24). This widely observed "aerosol invigoration of convection" corresponding to the dynamical effect of enhanced updraft velocity apparently contradicts cloud-resolving modeling studies that showed that only weak vertical wind shear and relatively humid conditions favor invigoration of convection by aerosols and enhance precipitation (6–8, 10).

To reconcile the observational and modeling results and examine how aerosols modify cloud macrophysical properties through changes on microphysics and convection, we conducted monthlong 3D simulations over two nested domains with two-way interactions for multiple summer convective systems over the tropics and midlatitude (Fig. 1). The outer domain was sized at ∼1,400 km, and the inner domain was at the cloud-resolving scale with ∼2-km grid resolution over ∼600 × 600 km (Fig. 1). Two sets of simulations were conducted, differing only in the initial aerosol concentrations by a factor of 6 to represent the clean and polluted environments. To explicitly simulate cloud microphysical processes and their interactions with aerosols and dynamics, we used a spectral-bin microphysics (SBM) parameterization for clouds where aerosols and hydrometeor species are represented using 33 size bins (13, 25, 26). These simulations used the dynamical framework of the Weather Research and Forecasting (WRF) model (27). More details about model setups are in *Materials and Methods*. These monthlong simulations that explicitly resolve convection and cloud microphysical processes and cover different summer convective systems are essential for deriving a more robust understanding of aerosol effects on DCCs, including the radiative feedbacks. We focused on aerosol effects by acting as CCN in this study. Aerosol direct radiative effects are not considered.

Simulations were performed over the tropical western Pacific (TWP), southeastern China (SEC), and the U.S. southern Great Plains (SGP) to represent tropical, midlatitude coastal, and midlatitude inland summer convective clouds, respectively. Over TWP and SEC, the atmosphere is generally humid with weak vertical wind shears, but SGP is relatively dry with strong vertical wind shears during most of the simulation period (Fig. 1) (clouds at SGP are generally organized by frontal systems). After day 21 in SGP, air is more humid, and vertical wind shear is a little weaker compared with the period before day 21. The basic cloud structure and convection timing were evaluated using ground-based observations, which are more accurate than satellite retrievals. Details on observational data are provided in *Materials and Methods*.

Results

At the SGP and TWP sites, the atmosphere is relatively clean with aerosol optical depth (AOD) for both in the range of 0.1–0.25, whereas AOD at SEC is more than 6 times larger in general (Fig. S1). The simulated cloud vertical structures (Fig. 2, left column) and diurnal variations of cloud frequency (Fig. 3) under the clean condition, which is closer to reality in TWP and SGP, agree remarkably well with observations there. Simulations under the polluted condition predict many more upper-level clouds and fewer low clouds compared with observations. In addition, the patterns of cloud diurnal variation predicted by the polluted simulations do not agree with observations as well as those from the clean runs. Better agreements in the time series hourly precipitation rate also are seen between the clean simulations and observations at these two sites (Fig. S2). In SEC, no observational data in cloud properties are available, but hourly precipitation data from a dense network of rain gauges are available for comparison. The averaged rain rate is not affected considerably by increasing aerosols (precipitation will be discussed more in the last part of this section). However, under the polluted condition, which is closer to reality in China, the simulation slightly outperforms the simulated clean condition. Capturing the diurnal variation of clouds and the time series of precipitation is key for partitioning SW and LW radiative forcing and determining the net radiative effect.

Enlarged Cloud Coverage, Increased Cloud Top Heights, and Cloud Thickness. Increasing aerosol concentrations by 6 times leads to an increase in cloud fraction, generally by 30%, in the upper troposphere in all three regions (Fig. 2), despite significant differences in the regions' dynamic and thermodynamic environ-

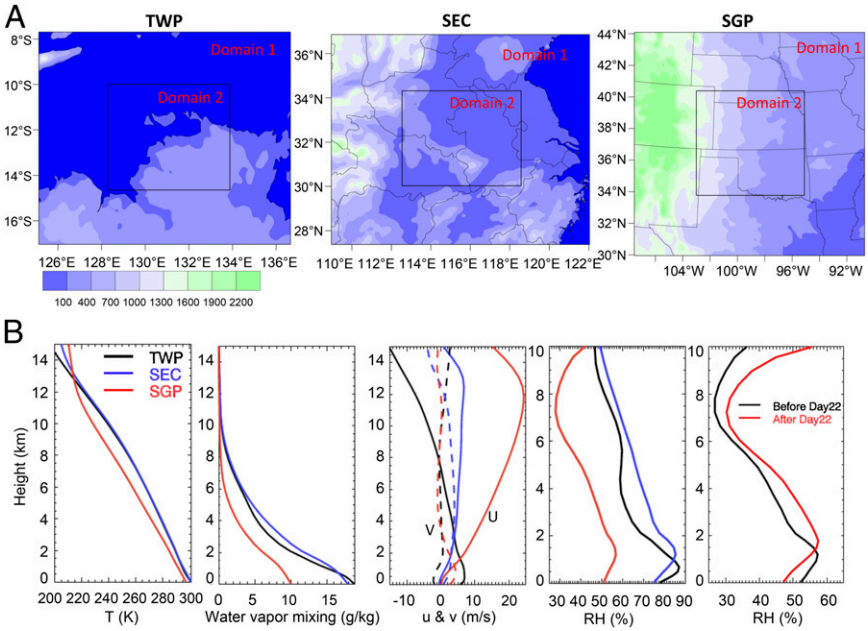

Fig. 1. Model domain and environment conditions. (*A*) The two nested domains for TWP, SEC, and SGP and (*B*) the vertical profiles of temperature (T), water vapor mixing ratio, wind components U (solid) and V (dashed), and RH for TWP (black), SEC (blue), and SGP (red) averaged over domain 2 and the simulation period. In SGP, the period after day 21 has higher RH (*B*, *Right*) and weaker wind shear compared with the preceding period. However, the wind shear is still stronger compared with TWP and SEC.

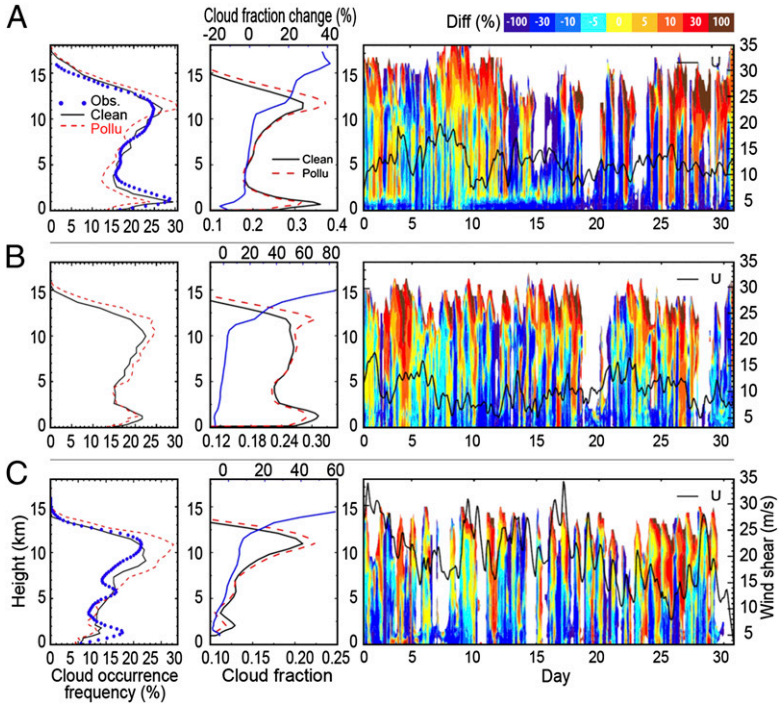

Fig. 2. Vertical profiles of cloud fraction for (*A*) TWP, (*B*) SEC, and (*C*) SGP. The left column shows the cloud occurrence frequencies during the 1-mo period at the ARM site from the clean (Clean; black) and polluted (Pollu; red dashed) simulations and observations (Obs; blue dotted) (there are no observed data for SEC). Cloud occurrence frequency at the site is calculated by the total number of cloudy counts during the 1-mo period divided by the total counts. The middle column shows the vertical profiles of cloud fractions averaged over the 1-mo simulation period. The percentage changes are shown as blue lines with the secondary *y* axis in the same plots. Cloud fraction is calculated by the number of cloudy points divided by the total number of points in the domain. Cloudy points are identified by total condensed water > 10^{-6} kg·kg^{-1}. The right column shows the time series of changes of cloud fractions in percentages at each vertical height from the clean and polluted conditions. The black lines in the right column are the zonal (U) wind shears calculated as (Maximum U − Minimum U) within 0–7 km.

ments. In SGP, the increase in cloud fraction before day 21 is less significant (>5%) than after day 21 (>30%) when RH is higher (Fig. 1) and vertical wind shear is relatively weaker (but still much stronger than in TWP and SEC; Fig. 1). Cloud fractions decrease in the lower troposphere consistently in all three regions. Separate examinations of the clouds at the convective core, stratiform/anvil, and shallow regimes indicate that the increase of cloud fraction in the upper troposphere occurs mainly in the stratiform/anvil rather than in the convective regime (Fig. 4). The increase in stratiform/anvil cloud fraction is seen both before and after day 21 in SGP, although RH and vertical wind shear differ between the two time periods. Because they are a very small part of the cloud coverage in the domain, the convective core areas change very little under simulations of clean to polluted environment conditions in all three regions, except for a small increase in TWP and SEC (with a relative change of ∼5% and 1%, respectively) and a ∼2% decrease in SGP.

Cloud fraction decreases in the lower troposphere because aerosols suppress shallow warm clouds (Fig. 4*C*). Note that the percentage decrease of cloud cover for all clouds in the lower levels is only 5–10% (Fig. 2), less than the reduction of the shallow warm clouds by over 20%, due to the increased cloud fraction of DCCs (shown later). Overall, for summer convection, aerosols increase cloudiness in the upper troposphere by expanding the stratiform/anvil area but suppress shallow clouds in the lower troposphere. Following our analysis in Li et al. (19), we analyzed cloud fractions for different types of cloud regimes from 10 y of observational data at SGP and show results consistent with our model simulations: cloud anvil fraction increases steadily with aerosol concentrations, but no consistent trend is observed for the convective cores (Fig. S3). A reduction in the fraction of shallow clouds with increasing aerosols is observed as well.

Accompanying the enlarged cloud fractions in the upper troposphere, CTH also increases consistently in all three regions. Fig. 5, left column, clearly shows a shift in frequency from low clouds toward high clouds under simulations from clean to polluted environments. The occurrence frequencies for clouds with CTH > 12 km are significantly higher in all regions. As indicated by the time series of CTH change (Fig. 5, right column), the CTH increase in TWP is the most significant and often exceeds 2 km. In SGP, although the increase of CTH before day 21 is not as significant as that in the period after, positive changes are still obvious. Separately examining the changes of CTH for the convective core and stratiform/anvil regimes, Fig. 6*A* shows small and inconsistent changes in the convective core area, whereas the stratiform/anvil regimes in all three regions show an increased frequency of higher clouds with CTH > 12 km in the polluted environment (Fig. 6*B*). These results suggest that the observed higher CTH in the polluted environment in past studies (19, 20) is contributed to mainly by the higher stratiform/anvil clouds rather than the convective cores.

Corresponding to the increased CTH in the stratiform/anvil regimes, the cloud thickness in those regimes is increased noticeably and consistent among the three regions (Fig. 6*D*), whereas the changes in convective cores are small and inconsistent (Fig. 6*C*). The increased CTH and cloud thickness in the polluted environment have also been observed in SGP for the summer deep clouds from long-term ground-based measurements (19) and in TWP from satellite measurements (20, 21). Therefore, our modeling simulations reproduced those observational features.

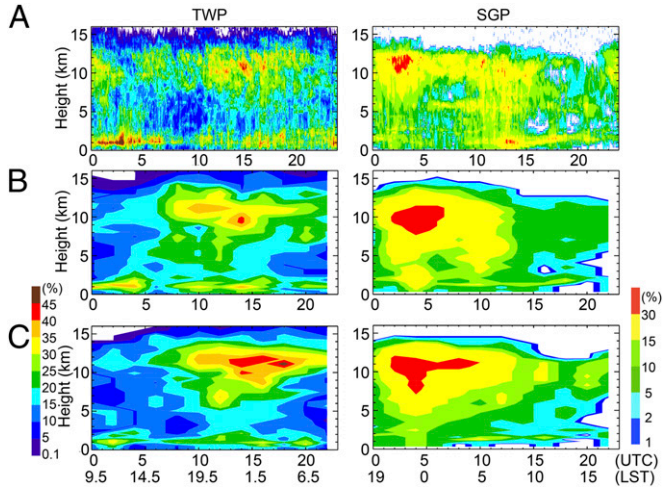

Fig. 3. Comparison of diurnal cycle of cloud occurrence frequency with observations averaged over the 1-mo simulation period for TWP and SGP. (*A*) Observations, (*B*) results of the clean simulation (Clean), and (*C*) results of the polluted simulation (Pollu). Both Coordinated Universal Time (UTC) and Local Standard Time (LST) are shown on the *x* axis. The clean condition simulations which approximate actual conditions at TWP and SGP agree much better with the observed diurnal variations of cloud occurrence frequency.

The Relative Roles of Dynamical and Microphysical Effects. We have indicated that the changes in cloud fraction, CTH, and cloud thickness from clean to polluted environments are small in the convective core area and that the direction of change is not even consistent. On the other hand, in the stratiform/anvil regimes, increases in cloud fraction, CTH, and cloud thickness are overwhelming and consistent in all three regions, even though environmental conditions are very different, spanning weak to strong wind shear and dry to humid conditions. These suggest that the dynamical effect related to enhanced updraft in the convective core (i.e., invigoration effect) may not be the leading cause of the overall increase in cloud fraction, CTH, and cloud thickness in polluted environments. To investigate this specifically, we examine quantities of in-cloud updraft mass fluxes (5, 7), updraft velocity (w), and updraft area in the lower and middle troposphere where strong convection occurs in DCCs (Fig. 7 *A*–*C*). We find that in TWP and SEC where vertical wind shears are weak and air is humid, the in-cloud updraft mass fluxes, w, and updraft area consistently increase by roughly 10–15%, 4–6%, and 5–10%, respectively, from clean to polluted environment simulations. In contrast, the in-cloud updraft mass fluxes and updraft area at 1–8 km are generally reduced by aerosols in SGP by about 3% and 5%, respectively, suggesting suppression of convection intensity by aerosols. In fact, the decreases of updraft mass flux and updraft area are more evident before day 21 when vertical wind shears are stronger. The invigoration of convection in TWP and SEC and the suppression in SGP are corroborated by the changes in convergence as shown in Fig. 7 *D* and *H*. The invigoration of DCCs in TWP and SEC and suppression in SGP by aerosols are consistent with our previous findings on the key role of vertical wind shear in aerosol invigoration effects (6, 7) and other modeling (8) and observational studies (19). Note that invigoration or suppression of the convection intensity by CCN is justified with the combination of in-cloud updraft mass flux, convergence, and updraft area, not with updraft velocity. The updraft velocity in all three cases is enhanced in the lower atmosphere from the clean to polluted environment (Fig. 7*C*), which is mainly due to enhanced condensational growth.

At the upper levels where stratiform/anvils reside (Fig. 7 *E*–*G*), the updraft mass fluxes in all three cases are increased due mainly to the large increases in updraft cloudy area since w is reduced in all three cases (~15% for TWP, 20% for SEC, and up to 45% in SGP). The increase of mass flux is especially large (~60% at 13 km) at SGP due to ~70% increase of updraft cloudy area (mainly from the period after day 21). The possible reasons for the reduced w in the upper-level clouds by aerosols are presented in *Discussion*.

Clearly, the increases in cloud fraction, CTH, and cloud thickness by aerosols are not determined by the dynamical effect or invigorated convection. In other words, regardless of humidity or dryness, weak or strong vertical wind shear, or whether convection is invigorated or not, cloud fraction, CTH, and cloud thickness increase from clean to polluted environments. An accompanying common characteristic is that the in-cloud updraft mass fluxes in the upper levels are increased by aerosols in all three cases due mainly to the expanded stratiform/anvil area rather than a stronger convection, especially given that in SGP the convection intensity is actually suppressed.

Because the dynamical factor of enhanced convection cannot explain the consistent increases in cloud fraction, CTH, and cloud thickness, we now turn to microphysical effects caused by aerosols. We note that in the polluted environment, ice crystal number concentrations in the convective core increase by a factor of 3–5 in the upper troposphere (>10 km) (Fig. S4) because of homogeneous freezing of the larger number of smaller droplets (Fig. 8*A*) lifted to higher altitudes by convection. Although ice mass concentrations also increase by up to a factor of 2 (Fig. S5), likely due to enhanced transformation of liquid to ice through the Wegener–Bergeron–Findeisen process (28, 29) when many more ice crystals are present, the size of the ice crystals still is reduced by up to 50% in the polluted environment.

Because stratiform/anvil clouds in the simulations can form only from the detrained hydrometeors from the convective cores (in situ cirrus clouds are not considered because our focus is DCC), the much increased cloud mass (more than 40%) from the clean to polluted conditions (Fig. S6*A*) and the larger stratiform/anvil cloud mass ratio (Fig. S6*B*) indicate that convective outflows deposit a greater amount of cloud mass to the

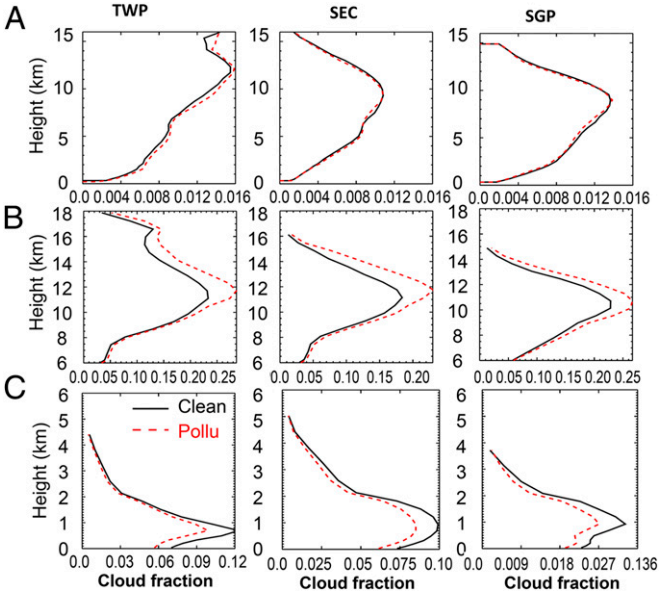

Fig. 4. Vertical profiles of cloud fractions in (*A*) the convective core area, (*B*) the stratiform/anvil regimes, and (*C*) the warm shallow clouds for TWP, SEC, and SGP under clean (black) and polluted (red dashed) conditions.

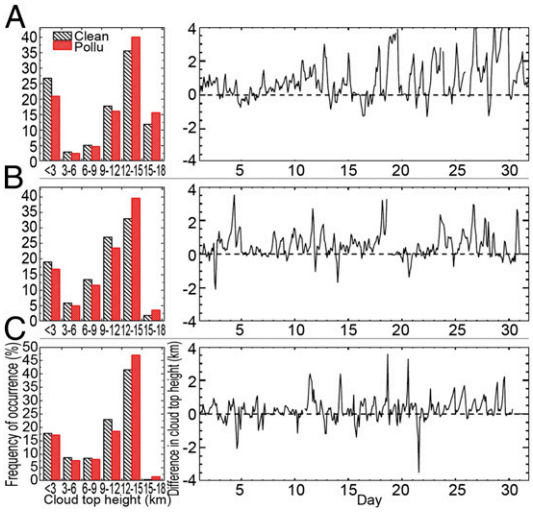

Fig. 5. CTH for (*A*) TWP, (*B*) SEC, and (*C*) SGP. The left column shows the occurrence frequency of clouds for different CTHs from the clean (black striped) and polluted (red) conditions. The right column shows time series of the differences in CTH between the polluted and clean conditions (polluted − clean). Positive (negative) values indicate increases (decreases) in CTH.

upper troposphere in the polluted environment. The ice and snow particle sizes are reduced almost by half (Fig. 8*B*) due to the much smaller droplets in polluted environments (reduced by approximately half as well; Fig. 8*A*). The reduction of ice and snow particle size leads to the reduction of their terminal velocities by up to a factor of 10 in the stratiform/anvil regime (Fig. 8*D*). Therefore, the fall velocities of ice and snow, which are the sum of the vertical velocity of air (upward positive) and the terminal velocities (downward positive), are reduced dramatically on average by 2.5 times compared with those in the clean environment (Fig. 8*C*). In the updraft area of the stratiform/anvil clouds, the particle fall velocities are near zero and can even be negative (Fig. 8*C*). Because fallout is a primary dissipation mechanism for cloud ice and snow in the stratiform/anvil clouds, reduced fall velocities due to the microphysical effects (i.e., changes in ice and snow particle size) greatly reduce the dissipation of stratiform/anvils. Even in the downdrafts, ice particles fall more slowly by a factor of 1.5 due to the reduced size (Fig. 8 *E* and *F*). The significant reduction in ice fall velocity as ice particle size decreases has been documented based on recent in situ aircraft measurements (30). Due to slow fallout, the stratiform/anvil clouds remain longer, and the strong horizontal advection in the upper troposphere further spreads them out over larger areas.

Fig. 9 vividly illustrates how the microphysical effects fundamentally determine the increase of CTH, cloudiness, and cloud thickness in polluted environments. Convective cores detrain a greater amount of cloud ice of much smaller size, leading to larger expansion and much slower dissipation of stratiform/anvil clouds because fall velocities of ice particles decrease noticeably with reduced particle size. This explains why observations consistently show increased cloud fraction, CTH, and cloud thickness, although convection intensity in the convective cores may or may not be enhanced by aerosols. Because wind shear in the upper troposphere (UT) controls anvil cloud cover and CTH is determined by the UT humidity (31), we examined the changes of wind components U and V and RH from the clean and polluted environments. In the middle and upper atmosphere, U and V are nearly unchanged, and RH changes are also very small and inconsistent among the three cases (slight increase in TWP but decrease in SEC). Therefore, both factors are excluded for explaining the consistent increase of cloud cover and top height of stratiform/anvils at the three locations. As illustrated in Fig. 9, clouds under the clean and polluted conditions may look similar at the developed stage as controlled by UT wind shear and humidity. However, due to much slower dissipation of stratiform/anvils under the polluted condition, clouds become much thicker and larger at the dissipation stage compared with the clean clouds (Fig. 9, bottom row), which are now controlled by cloud microphysics. This indicates that aerosol could modulate the large-scale dynamic controls on anvils through the microphysical effects after their developed stages.

Although it is very difficult to partition the contributions of convection intensity and the microphysical effect to the increased cloud fraction and CTH because of many interactions between them, for example, the microphysical effect that expands the anvils cools the surface and weakens the convection intensity. Here we present a first attempt to quantify them separately to gain some insights. The derivative of in-cloud updraft mass flux at each level can be calculated by

$$\mathrm{MF}' = \frac{\Delta \mathrm{MF}}{\Delta Z} \quad \text{where} \quad \Delta \mathrm{MF} = (\mathrm{MF}_k - \mathrm{MF}_{k+1}), \qquad [1]$$
$$\Delta Z = |Z_k - Z_{k+1}|.$$

Here MF represents the in-cloud updraft mass flux, which is calculated by vertical velocity × air density, and Z is the altitude for a specific vertical level k. The level at which the derivative of the in-cloud updraft mass flux (MF′) peaks is the central outflow height (COH). The difference in COH between the polluted and clean conditions represents the invigoration effect (IE) on CTH (negative value means suppression of convection). We define the IE on cloud fraction caused by aerosols as the ratio of MF at COH in the polluted to clean conditions. The total effect (TE) of aerosols on cloud fraction can be calculated as the ratio of cloud fractions in the polluted to clean conditions. Defining the microphysical effect (ME) as the amplification of cloud fraction due to microphysical changes (e.g., increased ice number but reduced

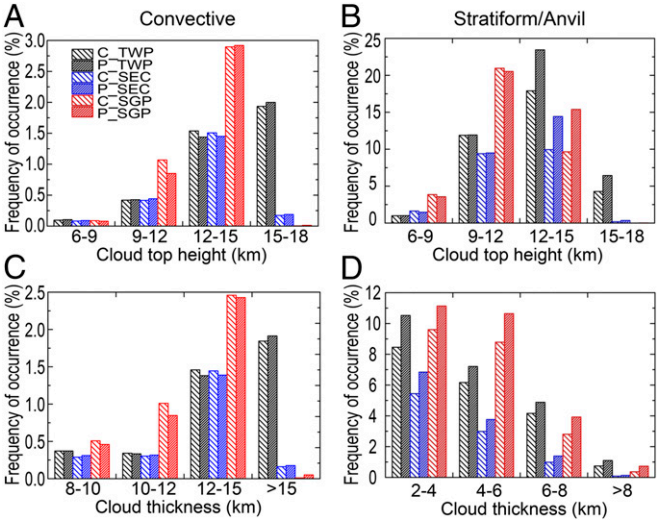

Fig. 6. Occurrence frequency of CTH and cloud thickness under clean (stripes) and polluted (densely filled bars) environments. The CTH for (*A*) the convective core area and (*B*) the stratiform/anvil regimes. (*C* and *D*) Cloud thickness. The occurrence frequency is calculated as the total number of grid points for a given bin (e.g., 12–15 km) divided by the total number of domain grid points during the 1-mo simulation period. It is an absolute because the total number of domain grid points does not change from the clean to polluted environments.

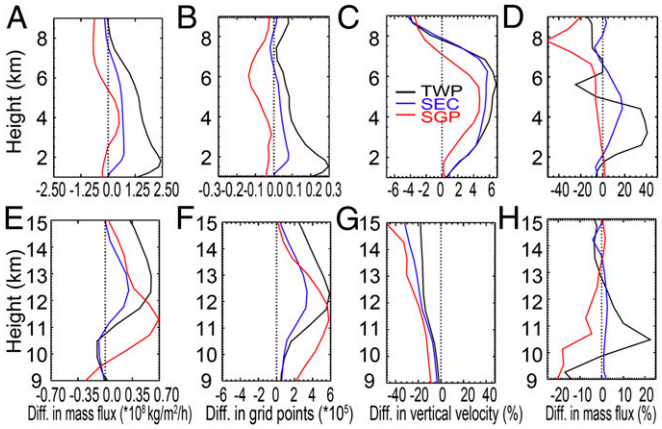

Fig. 7. Vertical profiles of the differences of (*A*) updraft mass fluxes, (*B*) number of updraft grid points, and (*C*) updraft velocity (w) between the polluted and clean conditions for TWP (black), SEC (blue), and SGP (red) from 1 to 9 km. (*E–G*) The same as *A–C* but for the 9- to 15-km altitude. Values in A–C are calculated on the cloudy points with $w > 1$ m·s^{-1} and on the cloudy points with $w > 0$ m·s^{-1} in *E–G*. (*D* and *H*) The corresponding horizontal mass fluxes (i.e., convergence × air density). The quantities shown for the lower and middle troposphere (*A–D*) indicate the convection intensity of DCCs. Use of $w > 1$ m·s^{-1} is to exclude the noise from natural variability and shallow clouds to better represent convection intensity. However, use of $w > 1$ m·s^{-1} at upper troposphere will exclude great amount of stratiform/anvil clouds; thus, $w > 0$ m·s^{-1} is used.

ice fall velocities) in cloud hydrometeors detrained by the enhanced MF, TE can be represented by

$$\mathrm{TE} = \mathrm{IE} \times \mathrm{ME} \quad \text{where} \quad \mathrm{TE} = \frac{f_p}{f_c}, \quad \mathrm{IE} = \frac{\mathrm{MF}_p}{\mathrm{MF}_c} \qquad [2]$$

Here ME is calculated based on Eq. **2** from IE and TE that are estimated from the simulations. f_p and f_c are the cloud fractions of DCCs in the polluted and clean conditions, respectively, and are calculated as the number of vertical columns occupied by DCCs including convective core and stratiform/anvil divided by the total number of columns in the simulation domain. MF_p and MF_c are the MF at COH in the polluted and clean environments, respectively.

On average, COH does not change from clean to polluted environments in TWP, SEC, and SGP before day 21 (Fig. 10*A*). This suggests that the invigoration effect on CTH induced by increasing CCN is negligible, which is likely because of buffering by the surface cooling induced by ME, and thus, ME is responsible for the increase of CTH in the stratiform/anvil. In SGP after day 21, IE contributes to a ∼0.6-km increase in CTH (Fig. 10*A*), and the average increase of CTH of DCCs is ∼1.7 km. Thus, ME is still dominant. In terms of effects on cloud fraction (Fig. 10*B*), the overall increase [calculated by $(\mathrm{TE}-1)\times 100$)] is 20% in TWP and SEC and 5% and 32% in SGP before and after day 21, respectively. The IE values in TWP, SEC, and SGP before day 21 are close to 1 (close to 0 in Fig. 10*B* because they are plotted as IE-1), indicating small changes of MF from the clean to polluted environments and thus a small IE on cloud cover by increasing CCN. We can calculate the contribution of IE to the expansion of cloud fraction by

$$\mathrm{IE}\% = \frac{\mathrm{IE}-1}{\mathrm{TE}-1} \times 100 \qquad [3]$$

then it is 26% in TWP and 27% in SEC. In SGP, the contribution is −35% before day 21 and −38% after day 21. Therefore, the maximum contribution of IE is only up to one-fourth in these cases. The zero or negative IE is likely because the atmosphere becomes more stable in the polluted condition due to the strong surface cooling resulted from ME. Therefore, ME is the dominant factor responsible for ∼3/4 of the 20% increase of cloud fractions in TWP and SEC and for the full increase in SGP. In fact, in SGP, ME compensates for the strong negative IE on cloud fraction (−35% before day 21 and −38% after day 21) from the clean to polluted conditions to obtain the overall increase. ME is especially large (1.5) after day 21 (Fig. 10*B*), considering the overall increase is still >30%. This approach, albeit being simple as it cannot separate the primary effect from its feedbacks, does show the dominant role of microphysical effects.

The shallow clouds in the polluted environment shown in Fig. 4*C* are prominently reduced by over 30%. The reduction is consistent in all three regions, whether convection is invigorated or not. It correlates well with the increased stratiform/anvil cloud fraction and thickness, possibly because the expanded and longer-living anvils shade more surface areas and inhibit their warming and development of shallow clouds. Stronger reduction in TWP and SEC also suggests that aerosol invigoration more deeply consumes the instability and cools the surface more strongly, thereby suppresses the low clouds. Past studies indicated that greater entrainment rates lead to a decrease of these clouds (32, 33). Because the grid resolution of this study is not very appropriate to examine entrainment and shallow clouds, the exact reasons warrant in-depth research in the future.

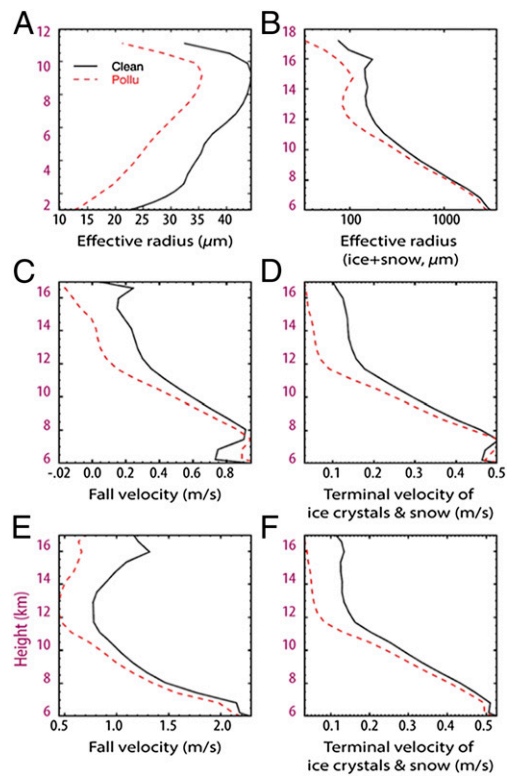

Fig. 8. Cloud microphysical properties for the clean (black) and polluted conditions (red). (*A*) Effective radius of liquid drops in the convective core area, (*B*) effective radius of ice and snow particles, (*C*) fall velocity of ice and snow particles, and (*D*) terminal velocity of ice and snow particles in the updraft area. (*E* and *F*) The same as *C* and *D* but for the downdraft area. *B–E* are for the stratiform/anvil clouds. Fall velocity is the sum of air motions (upward positive) and the terminal velocity (i.e., free fall) of the hydrometeors (downward positive).

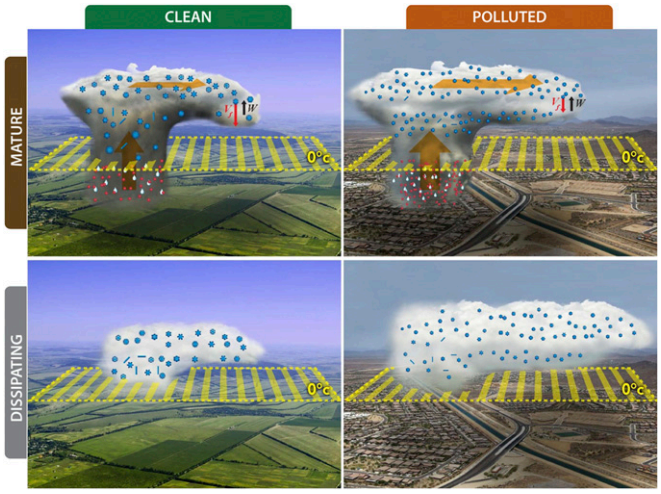

Fig. 9. Schematic illustration of the differences in CTH, cloud fractions, and cloud thickness for the storms in clean and polluted environments. Red dots denote cloud droplets, light blue dots represent raindrops, and blue shapes are ice particles. In the polluted environment, convective cores detrain larger amounts of cloud hydrometeors of much smaller size, leading to larger expansion and much slower dissipation of stratiform/anvil clouds resulting from smaller fall velocities of ice particles because of much reduced sizes. Therefore, the larger cloud cover, higher CTHs, and thicker clouds are seen in the polluted storm after the mature stage.

Radiative Forcing and Precipitation. Radiative impact is inevitably large because of the marked increases of cloud fractions, CTH, and cloud thickness, in addition to the increase in cloud albedo from clean to polluted environments. Good agreements in the simulated cloud vertical structure and timing of precipitation events with observations (Figs. 2 and 3 and Fig. S2) spanning multiple convective systems in each region give us confidence in the predicted radiative forcing. First, we notice a strong net surface cooling (5–8 $W{\cdot}m^{-2}$) from aerosol indirect effects and also a net cooling at TOA (2–4 $W{\cdot}m^{-2}$) consistent among the three regions (Fig. 10*C*). The cooling occurs mainly in the daytime (Fig. 10*D*). Larger cloud fractions, deeper clouds, and increased cloud albedo due to the smaller hydrometeor size all contribute to much stronger cooling during the daytime in the polluted environment. With larger and deeper clouds, we see a net warming effect on the atmosphere (3–5 $W{\cdot}m^{-2}$) because of longwave heating. At TOA and the surface, the daytime cooling effect of ∼10—18 $W{\cdot}m^{-2}$ overwhelms the warming effect, leading to the net cooling effect (Fig. 10*D*). At nighttime, the heating due to aerosol effects is about 5–7 $W{\cdot}m^{-2}$ at TOA and in the atmosphere. Note that the cooling of 5–8 $W{\cdot}m^{-2}$ at the surface and atmospheric warming of 3–5 $W{\cdot}m^{-2}$ are more significant than previous results derived at the storm scale (7). In addition, in this simulation, the TOA is cooling by 2–4 $W{\cdot}m^{-2}$ instead of warming as reported in Fan et al. (7). These differences are explained by a single storm system in Fan et al., in which most of the cloud lifetime occurred at night so LW heating dominated. Hence, our current study provides more robust statistical estimates of aerosol indirect effects based on larger samples of summer convective storms over three representative regions from long-term simulations.

The cooling during daytime and warming at night due to aerosol indirect effects reducing the diurnal temperature range by up to 1 K, which may significantly impact sea breeze-like circulations. The increasing of the daily minimum temperature by up to 0.6 K due to aerosol indirect forcing might be a contributor to the observed warming trend of the nighttime temperature during the past a few decades (34). The net cooling at TOA and the surface due to aerosol–DCC interaction may partially offset the warm temperature bias near the tropopause and at the surface over low-latitude and midlatitude land simulated by global models (35) that cannot realistically account for aerosol–DCC interactions. The net surface cooling by aerosol indirect effects would stabilize the atmosphere, leading to the small invigoration effect or even the suppression of convection in the long time basis over a large region. Similar results were shown in long time simulations of Morrison and Grabowski (15).

The radiative forcing values shown in Fig. 10 *C* and *D* have relatively small standard errors (SEs), indicating the significance of those values. The uncertainties from parameterizations of turbulence, microphysics, lateral boundary conditions, and other parameters could introduce the uncertainties to those radiative forcing values. However, we have tried to reduce those uncertainties as much as possible by using high-resolution long time simulations over three regions and the most explicit cloud microphysics.

The changes of average surface rain rate and total precipitation amount due to aerosol indirect effects are generally small and within a few percentage points (Fig. S7), similar to the results of other modeling studies (4, 5). Consistently among the three cases, stratiform rain amount is increased in the polluted environment (Fig. S6*D*), likely due to the larger amount of hydrometeors lifted to the upper level and detrained. However, the most significant change in precipitation by aerosols is the redistribution of rain rate. The occurrence frequency of light rain is reduced, but heavy rain in TWP and SEC becomes more frequent in polluted environments (Fig. S8*A*), whereas the changes at SGP differ before and after day 21. These findings are generally consistent with observational studies (19–23, 36) and further point to the aerosol effects on water cycle extremes like droughts and floods (19). The risk of droughts could increase with pollution in inland regions like the SGP where strong wind shears are frequent in convective clouds dominated by the frontal systems. At the same time, over the monsoon regions like

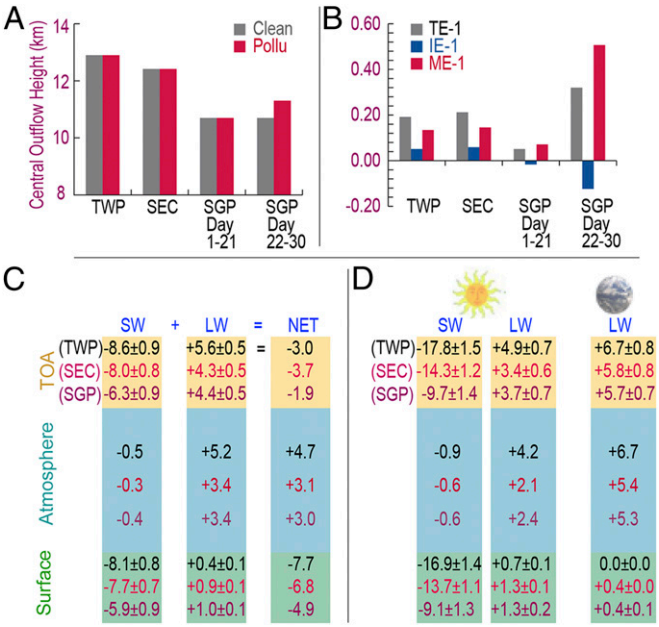

Fig. 10. Quantification results. (*A*) COH and (*B*) total effect (TE), invigoration effect (IE), and microphysical effect (ME). (*C* and *D*) Radiative forcing at top of atmosphere, atmosphere, and surface for TWP (black), China (red), and SGP (brown). The values shown in *B* are TE-1, IE-1, and ME-1. They are ratios with no unit. (*C*) Values averaged over the 1-mo simulation period and (*D*) values averaged over day and night. SE is shown.

China and northern Australia, the risk of both droughts and floods could be higher due to pollution.

Discussion

Through long time monthly simulations of typical summer convection at three regions with the most explicit cloud microphysical scheme to be as accurate as possible, we found that the fundamental determinants of the increases in cloud fractions, CTH, and cloud thickness are the microphysical effects. The invigoration of convection (24), which has been unanimously cited/hypothesized by observational studies to explain the increases, provides only partial explanation to the observations and in some cases cannot explain them at all. Within all cases, the maximum contribution of the dynamic aerosol invigoration is about one-fourth of the expansion of the anvils, as shown by the separation of the invigoration effect from the microphysical effects in this study. Therefore, it is important to combine the aerosol thermodynamic and microphysical effects to examine the impact of aerosols on the whole life cycle of a DCC system. The mechanisms revealed here validate the hypothesis from some observational studies that aerosols are responsible for the smaller ice particle size, larger cloud cover, and longer lifetime in polluted environments (20, 37–39). This study reconciles the apparent inconsistency between observational studies, which infer ubiquitous invigoration of convection by aerosols from observed increases in cloud fraction, CTH, and cloud thickness, and modeling studies that conclude that aerosol may or may not invigorate convection, depending on environmental conditions, especially wind shear. In addition, our results with SBM support those from the two-moment bulk microphysics scheme in Morrison and Grabowski (15).

The predominant microphysical effects of aerosols on stratiform/anvil macroproperties and microproperties have significant implications on climate forcing and circulation because stratiform/anvil clouds cover large areas and last much longer than the convective cores. Hence, this study calls for an augmented focus on understanding stratiform/anvils associated with the mature phase of the convective life cycle. Because current weather and climate models do not yet include cloud microphysics and aerosol–cloud interactions in deep convection parameterizations, the warming at the surface could be overestimated by current models of the Intergovernmental Panel on Climate Change, considering the strong net cooling (5–8 $W \cdot m^{-2}$ here) at the surface estimated in this study that can be produced by aerosol effects.

The surface cooling combined with atmospheric warming could produce a stabilization effect that counters aerosol invigoration, which might explain the weak invigoration effect quantified in this study using a more realistic large domain. Such an effect is likely not captured in previous cloud-resolving scale-modeling studies that used a small domain for a short time period or coarse-scale modeling in which convection microphysics are not appropriately represented. Therefore, over a large region and long time period, the dynamical invigoration effect on DCCs by increasing aerosols is buffered partially by the feedback of radiative forcing to the system, leaving the microphysical effect to dominate the changes on the cloud properties.

Most previous studies concentrated on aerosol effects on convection intensity (e.g., refs. 6, 14 and 24). For summer deep convection clouds, convection intensity is generally very strong, and hence, the potential influence of aerosols on the vertical development of convective cores is limited. However, the changes on stratiform/anvils by microphysical effects are of far more importance to the radiative forcing as calculated in this paper. Many past modeling studies examined vertical velocity and used it as an indicator for whether convection is enhanced or suppressed by aerosols. Fig. 7 shows that by looking at the vertical velocity alone (Fig. 7*C*), convection below 7 km is enhanced in all three regions, likely due to enhanced condensational growth in the polluted environment. However, in-cloud updraft mass flux, updraft area, and convergence (Fig. 7 *A*, *B*, and *D*) in SGP are reduced in the polluted environment. Their reduction is especially significant before day 21 in SGP where vertical wind shear is very strong. Therefore, extra care should be exerted in determining convection strength. We find that the increasing trends of in-cloud updraft mass flux, updraft area, and convergence in the lower and middle troposphere along with increased heavy rain frequency and amount are more reliable indicators of aerosol invigoration effects. Limited by measurable quantities, observational studies used surface precipitation, cloud fraction, CTH, or cloud thickness as indicators of convection intensity. This study, however, suggests that the increase of those quantities does not necessarily reflect invigoration of convection.

The aerosol-induced reduction in updraft vertical velocity in the upper-level clouds seems to contradict the hypothesis that updraft vertical velocity should be increased because more latent heat is released from freezing of larger amounts of cloud water. Our exanimation shows that although latent heat above 8 km is increased in the convective core area in the polluted case (the increase peaks around 10 km at the homogeneous freezing level) due primarily to freezing and deposition growth of ice particles, the eddy diffusion [turbulence kinetic energy (TKE)] as shown in Fig. S9 is also increased by a factor of up to 2 above 11 km, indicating stronger mixing with environment. This likely contributes to the decreased vertical velocity in the polluted environment. The large increase in TKE at the upper levels is likely because of the increase of vertical temperature gradient that resulted from the significant changes to radiative forcing caused by microphysical effects. On the other hand, in the clean environment, the much larger fall velocities of cloud ice and snow at upper levels could produce stronger downdrafts, which would induce stronger updrafts relative to the polluted environment.

Very recent idealized modeling studies with bulk microphysics parameterization in radiative–convective equilibrium conditions for tropical convection produced different results compared with this study. CCN were shown to both increase (16) and decrease (17) the high-level cloud fraction. Because the changes are not large, both studies claimed that cloud fraction is not sensitive to CCN. The latter study also showed that both SW and LW radiative forcings at the TOA decreased with increasing CCN (17). We investigated why bulk schemes did not produce the same results as our bin model in a separate study. As shown in Fig. S10, the Morrison bulk scheme that was used in Khairoutinov and Yang (17) could not simulate the much reduced fall velocities of ice and snow at the upper levels from clean to polluted conditions, which is the key factor resulting in slow cloud dissipation and increased cloud fraction, CTH, and cloud thickness that are found in both ground-based multisensor and satellite measurements (12, 19–21). Bulk schemes cannot inherently simulate such effects because they do not calculate a spectrum of particle size-resolved fall speeds within each model grid box. This is a main distinction between bulk and bin-resolving microphysical schemes that makes the latter much more computationally expensive and limits their use in climate simulations. Therefore, accurately representing cloud microphysics, which is achieved using the bin model in this study, is key to understanding the fundamental mechanisms behind the observed phenomena.

We admit that there are always some model uncertainties. We have tried to reduce some uncertainties by using long time simulations over a few regions, the most explicit cloud microphysics, open lateral boundary conditions, and a high-resolution ~2-km grid to resolve deep convective clouds at the expense of huge computation time. Uncertainty from model formulations may be large, posing the need to rigorously evaluate their per-

formance against observation data. In this regard, the close agreements of cloud fractions and vertical structures between modeled results and observations and the reproduction of the increased cloud fraction, CTH, and cloud thickness by aerosols observed in many studies (12, 19–21) help lend us confidence that the SBM used in this study does a reasonable job. Even at the resolution of ∼2 km used in this study, some uncertainties may remain in capturing detrainment because the convective cores may be too adiabatic, lift too much cloud liquid water to high levels (40), and overestimate the microphysical effects. Note that the undiluted convective core is a common feature in simulations that use bulk microphysics even when the models are applied at 1-km to 500-m resolutions (41). This may be primarily because the saturation adjustment method removes supersaturation in a single time step, which is very short at high spatial resolution, and artificial freezing of large rain drops is caused by the use of the fixed gamma distribution for rain drops. Despite the various uncertainties discussed above, validation of our simulations of clouds and precipitation with observations in this study and in a few of our previous studies (e.g., ref. 13) indicate that the bin model applied at 2-km resolution can adequately capture convective cloud systems. The resolution might be too coarse for shallow clouds, but they are not the targets of this study.

Our current understanding of microphysical processes such as ice nucleation and the relationships between the ice/graupel/hail fall velocity/density and their sizes is still limited; therefore, the uncertainties from these aspects could be large. As for ice nuclei, our previous simple tests indicated that ice nuclei may have little effect on convective strength but can increase ice number and mass concentrations in stratiform/anvils significantly (42) and enhance the microphysical effects. There is also uncertainty from the exclusion of aerosol direct effect, although under the strong updraft environment, aerosol indirect effect likely overrides the direct effect under most conditions (except for pure black carbon/soot aerosols). For strongly absorbing aerosols, studies in the literature showed a suppression effect on convection due to the stabilization effect from the lower-level heating (43).

Materials and Methods

Model Setup. Simulations were performed using the WRF model version 3.2 developed at the National Center for Atmospheric Research (27). The WRF model was coupled with a fast version of SBM in which every species is represented by 33 mass doubling bins; that is, the mass of a particle m_k in the kth bin is determined as $m_k = 2\ m_{k-1}$ (13, 25, 26). All relevant microphysical processes/interactions, including droplet nucleation, primary and secondary ice generation, condensation/evaporation of drops, deposition/sublimation of ice particles, freezing/melting, and mutual collisions between the various hydrometeors, were calculated explicitly. Heterogeneous and homogeneous droplet freezing was calculated according to Bigg parameterization (44). Deposition/condensation ice nucleation used the parameterizations of Meyers et al. (45). Homogeneous freezing of aerosols for in situ cirrus clouds was ignored in this study because our focus was on DCCs and also because the ice nucleation mechanism of cirrus clouds is still controversial (46). Ice nucleation parameterizations and mechanisms are undergoing significant changes due to instrumental progress in recent years. Because the simulations for this study were started 2–3 y ago, we did not try the new ice nucleation parameterizations/mechanisms due to the very expensive computational cost that would have been incurred. We believe that the uncertainty from ice nucleation parameterizations would not change our results qualitatively.

Simulations of real cases were performed with two domains two-way nested over three regions (TWP, SEC, and SGP; Fig. 1). The horizontal resolutions were ∼10 km and ∼2 km for domains 1 and 2, respectively (for the SEC case, resolutions of 12 km and 2.5 km were used). The domain horizontal size was ∼1,400 km for domain 1 and 600 km for domain 2. There are 41 vertical levels, with resolutions ranging from 70 m to 800 m from the lowest to the highest levels. The large domain size and the two-way interactions between the two domains were used to provide a more representative view of the effects at the regional scale. Data from the Nation Centers for Environmental Prediction Final Operational Global Analysis, recorded continuously every 6 h on a 1° × 1° grid, provided the initial and boundary conditions for domain 1. The Grell–Devenyi cumulus parameterization (47) was used in domain 1. Other physics schemes used in the simulations include the Noah land surface model (48), the Yonsei University planetary boundary layer scheme (49), and the rapid radiative transfer model (RRTM) for general circulation model (GCM) shortwave and longwave radiation schemes (50) with effective radius calculated based on the predicted size distributions calculated by the cloud microphysics scheme. For each region, simulations were conducted for clean and polluted conditions (referred to as "Clean" and "Pollu," respectively), with CCN concentrations of 280 cm^{-3} and 6 × 280 cm^{-3}, respectively, at the initial time step. The initial CCN size spectra are determined by the power law relationship $n = cS^k$ as described in ref. 13. The parameter c is to set be 100 and 600 cm^{-3} for clean and polluted conditions, respectively, and k is 0.308 for both conditions. The obtained size spectrum is then decomposed into 33 bins ranging from 2 nm to 2 μm. CCN in each bin are prognostic during the simulations. Aerosol loading was increased only in the inner domain. Note that the prescribed initial CCN only denote the gross conditions of clean and polluted environments that are very distinct among the three sites under study (Fig. S1). It is not realistic to include aerosol and chemistry processes in simulations with SBM for monthlong runs and over a large domain to simulate the real aerosol conditions. In addition, introducing aerosol/chemistry processes could introduce more uncertainties because aerosol representations are very uncertain; for instance, different mixing assumptions (i.e., external vs. internal) can give very different aerosol properties.

The simulations were run for 1 mo each. For TWP, the time period was January 16 through February 15, 2006, covering the active monsoon and monsoon break periods during the TWP-International Cloud Experiment (ICE) field campaign (51). For SEC, the simulation period was July 2008 during the U.S. Department of Energy Atmospheric Radiation Measurements (ARM) Mobile Facility-China field campaign (13). June 2008 was the period for SGP, which is one of the permanent observational sites of the ARM program. Because large model domains were used to capture the large convective systems and estimate the effects on the regional scale and SBM is computationally very expensive, the model was reinitialized every 2 d; each reinitialization run simulated 2 d and 6 h, and the initial 6 h were excluded from the analysis. Model outputs were archived every 2 h for analysis. The simulations were completed using several million node hours on a large Linux cluster with 14,592 cores (122 teraflops peak) at the Pacific Northwest National Laboratory to achieve CRM simulations with explicit cloud microphysics to realistically simulate convective cloud systems and aerosol effects over large regions.

Convective core areas in the model simulations were identified using the following criteria: (*i*) cloud bases are below the melting level, (*ii*) single-layer cloud thickness is >8 km, and (*iii*) vertical velocity (w) is larger than 1 $m{\cdot}s^{-1}$. We used $w > 1\ m{\cdot}s^{-1}$ to strictly limit the core updraft area so that it would better reflect aerosol impact on convection intensity. After the convective core areas were identified, the remaining single-layer clouds with the existence of cloud ice and with the cloud base higher than the melting levels were identified as stratiform/anvil regimes (52, 53). We conducted a careful check on snapshot figures to ensure that those criteria were sufficient to identify convective cores and the corresponding stratiform/anvil areas. In situ cirrus clouds were not considered in the simulations to avoid introducing additional uncertainty because our target for this study was DCC. The term "warm shallow clouds" refers to liquid clouds only, with the CTH below the melting level.

Observational Analysis. For the analyses of the TWP and SEC regions, we used Active Remotely Sensed Clouds Locations (ARSCL) data for cloud fractions. The data are available at each vertical level from 100 m to 15,900 m at 200-m intervals from the ARM Climate Model Best Estimate product. The time frequencies of the data are 10 s. With this dataset, we examined the observed vertical profiles of cloud occurrence frequency and compared them with model simulations (Fig. 2). No observational data in cloud properties are available for SEC. To examine if the model captured the deep convective systems, we compared the simulated precipitation time series with the observed. Precipitation data are available for SEC from rain gauges gridded at a 10 km × 10 km resolution. Precipitation data for the SGP region came from the Arkansas-Red Basin River Forecast Center. These data have been extensively quality controlled and are available as ARM Value-added Products (VAP) at hourly intervals and a 4-km resolution derived from a combination of Weather Surveillance Radar, 1988, Doppler (WSR-88D) radar precipitation estimates and rain gauge reports. For the TWP, we used the precipitation data in the ARM standard variational analysis data (54), which are from the C-band polarimetric/Doppler meteorological radar system (C-POL) retrieved rain rate. The data represent an average over the analysis domain as shown in (55), and the model data shown in Fig. S2 are averaged over the same region. The changes in precipitation rate averaged over the domain are

small from the clean to polluted conditions with a few percentage points of increase in TWP and SEC and a slight decrease in SGP before day 21.

Our previous observational analyses at SGP have shown the increase of CTH and cloud thickness for the summer DCCs at SGP (19) as aerosol increases. Following that, we examined the cloud fractions for DCC core clouds, anvil clouds, and shallow clouds as shown in Fig. 4. The yellowish-green is for the DCC core area. Cloud fractions were calculated by the ratio of the number of cloudy pixels to that of total pixels in the 20 km × 20 km field of view centered at the central facility site of the SGP for an identified DCC. DCC is identified with single-layer clouds with a cloud base temperature > 15 °C and cloud top temperature < −4 °C using the ARM ARSCL VAP for the SGP site (19). The data over the domain are from Geostationary Operational Environmental Satellite pixel retrieval products. For DCCs, we separated them further into a thick core part [pixels with cloud optical depth (τ) > 10] and an anvil part with $\tau < 10$.

The results shown here were obtained from 10 y of continuous measurements from 2000 through 2010. Note that the definitions of DCC core and anvil areas and the calculation of cloud fraction from the limited observational data may not be consistent with those from our model simulations, but the qualitative insight is provided. The question remaining is how to better identify different types of clouds, especially DCCs, from the observations in this field.

ACKNOWLEDGMENTS. This study was supported by the US Department of Energy (DOE) Office of Science Biological and Environmental Research as part of Atmospheric Sciences Research Program (ASR) and the Regional and Global Climate Modeling Program, and the Ministry of Science and Technology of China under its National Key Program on Global Changes (2013CB955804 and 2012CB955301). The Pacific Northwest National Laboratory (PNNL) is operated for DOE by Battelle Memorial Institute under Contract DE-AC05-76RL01830. D.R. and Z.L. are also supported by DOE ASR. Additional sponsors to Z.L. are National Science Foundation and National Aeronautics and Space Administration. The research used data from the DOE Atmospheric Radiation Measurement Climate Research Facility. The model simulations were performed using PNNL Institutional Computing.

1. Arakawa A (2004) The cumulus parameterization problem: Past, present, and future. *J Clim* 17(13):2493–2525.
2. Futyan JM, Del Genio AD (2007) Deep convective system evolution over Africa and the tropical Atlantic. *J Clim* 20(20):5041–5060.
3. Solomon S, et al. (2007) Technical summary. *Climate Change 2007: The Physical Science Basis*, eds Solomon S, et al. (Cambridge Univ Press, Cambridge, UK), pp 19–91.
4. Tao W-K, Chen J-P, Li Z, Wang C, Zhang C (2012) Impact of aerosols on convective clouds and precipitation. *Rev Geophys* 50(2):RG2001.
5. Morrison H (2012) On the robustness of aerosol effects on an idealized supercell storm simulated with a cloud system-resolving model. *Atmos Chem Phys* 12(16):7689–7705.
6. Fan J, et al. (2009) Dominant role by vertical wind shear in regulating aerosol effects on deep convective clouds. *J Geophys Res* 114(D22):D22206.
7. Fan J, Rosenfeld D, Ding Y, Leung LR, Li Z (2012) Potential aerosol indirect effects on atmospheric circulation and radiative forcing through deep convection. *Geophys Res Lett* 39(9):L09806.
8. Khain AP, BenMoshe N, Pokrovsky A (2008) Factors determining the impact of aerosols on surface precipitation from clouds: An attempt at classification. *J Atmos Sci* 65(6):1721–1748.
9. Tao W-K, et al. (2007) Role of atmospheric aerosol concentration on deep convective precipitation: Cloud-resolving model simulations. *J Geophys Res* 112(D24):D24S18.
10. Seifert A, Beheng KD (2006) A two-moment cloud microphysics parameterization for mixed-phase clouds. Part 2: Maritime vs. continental deep convective storms. *Meteorol Atmos Phys* 92(1):67–82.
11. van den Heever SC, et al. (2006) Impacts of nucleating aerosol on Florida storms. Part I: Mesoscale simulations. *J Atmos Sci* 63(7):1752–1775.
12. Zhang R, Li G, Fan J, Wu DL, Molina MJ (2007) Intensification of Pacific storm track linked to Asian pollution. *Proc Natl Acad Sci USA* 104(13):5295–5299.
13. Fan J, et al. (2012) Aerosol impacts on clouds and precipitation in eastern China: Results from bin and bulk microphysics. *J Geophys Res* 117(D16):D00K36.
14. Lebo ZJ, Seinfeld JH (2011) Theoretical basis for convective invigoration due to increased aerosol concentration. *Atmos Chem Phys* 11(11):5407–5429.
15. Morrison H, Grabowski WW (2011) Cloud-system resolving model simulations of aerosol indirect effects on tropical deep convection and its thermodynamic environment. *Atmos Chem Phys* 11(20):10503–10523.
16. van den Heever SC, Stephens GL, Wood NB (2011) Aerosol indirect effects on tropical convection characteristics under conditions of radiative–convective equilibrium. *J Atmos Sci* 68(4):699–718.
17. Khairoutdinov MF, Yang CE (2013) Cloud-resolving modelling of aerosol indirect effects in idealised radiative-convective equilibrium with interactive and fixed sea surface temperature. *Atmos Chem Phys* 13(8):4133–4144.
18. Andreae MO, et al. (2004) Smoking rain clouds over the Amazon. *Science* 303(5662): 1337–1342.
19. Li Z, et al. (2011) Long-term impacts of aerosols on the vertical development of clouds and precipitation. *Nat Geosci* 4(12):888–894.
20. Koren I, Remer LA, Altaratz O, Martins JV, Davidi A (2010) Aerosol-induced changes of convective cloud anvils produce strong climate warming. *Atmos Chem Phys* 10(10): 5001–5010.
21. Niu F, Li Z (2012) Systematic variations of cloud top temperature and precipitation rate with aerosols over the global tropics. *Atmos Chem Phys* 12(18):8491–8498.
22. Bell TL, et al. (2008) Midweek increase in U.S. summer rain and storm heights suggests air pollution invigorates rainstorms. *J Geophys Res* 113(D2):D02209.
23. Koren I, et al. (2012) Aerosol-induced intensification of rain from the tropics to the mid-latitudes. *Nat Geosci* 5(2):118–122.
24. Rosenfeld D, et al. (2008) Flood or drought: How do aerosols affect precipitation? *Science* 321(5894):1309–1313.
25. Khain A, Pokrovsky A, Pinsky M, Seifert A, Phillips V (2004) Simulation of effects of atmospheric aerosols on deep turbulent convective clouds using a spectral microphysics mixed-phase cumulus cloud model. Part I: Model description and possible applications. *J Atmos Sci* 61(24):2963–2982.
26. Khain A, Lynn B (2009) Simulation of a supercell storm in clean and dirty atmosphere using weather research and forecast model with spectral bin microphysics. *J Geophys Res* 114(D19):D19209.
27. Skamarock WC, et al. (2008) *A Description of the Advanced Research WRF Version 3* (Natl. Cent. for Atmos. Res., Boulder, CO).
28. Korolev AV, Mazin IP (2003) Supersaturation of water vapor in clouds. *J Atmos Sci* 60(24):2957–2974.
29. Fan J, et al. (2011) Representation of Arctic mixed-phase clouds and the Wegener-Bergeron-Findeisen process in climate models: Perspectives from a cloud-resolving study. *J Geophys Res* 116(D1):D00T07.
30. Mitchell DL, Mishra S, Lawson RP (2011) Representing the ice fall speed in climate models: Results from Tropical Composition, Cloud and Climate Coupling (TC4) and the Indirect and Semi-Direct Aerosol Campaign (ISDAC). *J Geophys Res* 116(D1):D00T03.
31. Hartmann DL, Larson K (2002) An important constraint on tropical cloud - climate feedback. *Geophys Res Lett* 29(20):1951.
32. Altaratz O, Koren I, Reisin T, Kostinski A, Feingold G, Levin Z, Yin Y (2008) Aerosols' influence on the interplay between condensation, evaporation and rain in warm cumulus cloud. *Atmos Chem Phys* (8):15–24.
33. Xue H, Feingold G (2006) Large-eddy simulations of trade wind cumuli: Investigation of aerosol indirect effects. *J Atmos Sci* 63(6):1605–1622.
34. Nemani RR, et al. (2001) Asymmetric warming over coastal California and its impact on the premium wine industry. *Clim Res* 19(1):25–34.
35. Xie S, Ma H-Y, Boyle JS, Klein SA, Zhang Y (2012) On the correspondence between short- and long-time-scale systematic errors in CAM4/CAM5 for the year of tropical convection. *J Clim* 25(22):7937–7955.
36. Qian Y, et al. (2009) Heavy pollution suppresses light rain in China: Observations and modeling. *J Geophys Res* 114(D7):D00K02.
37. Lindsey DT, Fromm M (2008) Evidence of the cloud lifetime effect from wildfire-induced thunderstorms. *Geophys Res Lett* 35(22):L22809.
38. Rosenfeld D, et al. (2007) The Chisholm firestorm: Observed microstructure, precipitation and lightning activity of a pyro-cumulonimbus. *Atmos Chem Phys* 7(3):645–659.
39. Sherwood SC, Phillips VTJ, Wettlaufer JS (2006) Small ice crystals and the climatology of lightning. *Geophys Res Lett* 33(5):L05804.
40. Fan J, Comstock JM, Ovchinnikov M (2010) The cloud condensation nuclei and ice nuclei effects on tropical anvil characteristics and water vapor of the tropical tropopause layer. *Environ Res Lett* 5(4):044005.
41. Bryan GH, Morrison H (2011) Sensitivity of a simulated squall line to horizontal resolution and parameterization of microphysics. *Mon Weather Rev* 140(1):202–225.
42. Varble A, et al. (2011) Evaluation of cloud-resolving model intercomparison simulations using TWP-ICE observations: Precipitation and cloud structure. *J Geophys Res* 116(D12):D12206.
43. Fan J, Zhang R, Tao W-K, Mohr KI (2008) Effects of aerosol optical properties on deep convective clouds and radiative forcing. *J Geophys Res* 113(D8):D08209.
44. Bigg EK (1953) The formation of atmospheric ice crystals by the freezing of droplets. *Q J R Meteorol Soc* 79(342):510–519.
45. Meyers MP, DeMott PJ, Cotton WR (1992) New primary ice-nucleation parameterizations in an explicit cloud model. *J Appl Meteorol* 31(7):708–721.
46. Cziczo DJ, et al. (2013) Clarifying the dominant sources and mechanisms of cirrus cloud formation. *Science* 340(6138):1320–1324.
47. Grell GA, Dévényi D (2002) A generalized approach to parameterizing convection combining ensemble and data assimilation techniques. *Geophys Res Lett* 29(14):1693.
48. Chen F, Dudhia J (2001) Coupling an advanced land surface–hydrology model with the Penn State–NCAR MM5 modeling system. Part I: Model implementation and sensitivity. *Mon Weather Rev* 129(4):569–585.
49. Hong S-Y, Noh Y, Dudhia J (2006) A new vertical diffusion package with an explicit treatment of entrainment processes. *Mon Weather Rev* 134(9):2318–2341.
50. Iacono MJ, et al. (2008) Radiative forcing by long-lived greenhouse gases: Calculations with the AER radiative transfer models. *J Geophys Res* 113(D13):D13103.
51. May PT, Allen G, Vaughan G, Connolly P (2009) Aerosol and thermodynamic effects on tropical cloud systems during TWPICE and ACTIVE. *Atmos Chem Phys* 9(1):15–24.
52. Frederick K, Schumacher C (2008) Anvil characteristics as seen by C-POL during the Tropical Warm Pool International Cloud Experiment (TWP-ICE). *Mon Weather Rev* 136(1):206–222.
53. Fan J, et al. (2010) Tropical anvil characteristics and water vapor of the tropical tropopause layer: Impact of heterogeneous and homogeneous freezing parameterizations. *J Geophys Res* 115(D12):D12201.
54. Xie S, et al. (2010) Observed large-scale structures and diabatic heating and drying profiles during TWP-ICE. *J Clim* 23(1):57–79.
55. Fridlind AM, et al. (2012) A comparison of TWP-ICE observational data with cloud-resolving model results. *J Geophys Res* 117(D5):D05204.